PHYSICAL REVIEW C VOLUME 49, NUMBER 4 APRIL 1994

Competing reaction mechanisms for the ^{16,17,18}O+^{10,11}B and ^{19}F+ ^{9}Be systems

R. M. Anjos, N. Added, N. Carlin, L. Fante, Jr., M. C. S. Figueira, R. Matheus, E. M. Szanto, C. Tenreiro, and A. Szanto de Toledo
Departamento de Física Nuclear, Instituto de Física da Universidade de São Paulo, Caixa Postal 20516, 01458-990 São Paulo, Brasil

S. J. Sanders
Department of Physics and Astronomy, The University of Kansas, Lawrence, Kansas 66045

(Received 24 September 1993)

Fusion, strongly damped, quasielastic and elastic scattering yields have been measured for the ^{16,17,18}O+^{10,11}B systems at 1 MeV $\leq E/A \leq$ 4 MeV and ^{19}F+^{9}Be at 56 MeV. The significant yields observed for the strongly energy-damped products are attributed to a fusion-fission process. This identification is supported by statistical model calculations based on the transition-state model of fission. The elastic scattering data present enhanced back-angle yields which can be understood in terms of a compound elastic process. These results help to further establish the reaction systematics in this mass region.

PACS number(s): 25.70.Jj, 25.70.Gh, 25.70.Lm

I. INTRODUCTION

Fusion reactions involving light heavy ions present many new and interesting features [1–15]. Despite the systematic investigations of these reactions during the past two decades, many of the questions regarding the limitation of complete-fusion cross sections, the relationship between the gross features of the reaction data and the structure of the involved nuclei, and the characteristics that act as signatures of the competing reaction mechanisms remain uncertain [16]. The difficulty in dealing with these global features is that for light ions, where the binding energy per nucleon has yet to reach saturation ($B/A \leq 8$ MeV), the single-particle characteristics dominate over the macroscopic features of nuclei, thus obscuring the systematic behaviors. At the same time, valence nucleons are found to have a dramatic influence on the competition between open reaction channels. Additional difficulties arise in the characterization of the competing processes experimentally because of the ambiguities associated with the kinematics for different reaction mechanisms. For example, different processes may populate exit channels with a given atomic number, mass, and energy. The lack of microscopic models able to supply a systematic description of the effects of the nuclear structure on the fusion cross section of these light nuclei reflects the complexity of the problem.

In this work we present a systematic study of the ^{16,17,18}O+^{10,11}B and ^{19}F+^{9}Be reactions. Detailed measurements of atomic number and mass distributions of all charge particle channels with $Z > 2$, including the evaporation-residue, binary-reaction, and elastic-scattering channels, were performed. Coincidence measurements and velocity distribution measurements were used to confirm the binary nature of the reaction yields.

The specific choice of reactions to investigate was based on three primary considerations. First, by using reverse kinematics, the significant entrance-channel mass asymmetries

$$\eta = (A_{\text{heavy}} - A_{\text{light}})/(A_{\text{heavy}} + A_{\text{light}})$$

of these systems allow for clear identification of the targetlike products emitted at large center-of-mass angles. These reaction products, which are detected at forward laboratory angles, can be associated with long-lived intermediate configurations of the compound system [15]. Second, a large number of nuclear systems can be investigated using these reactions with small variation of the entrance-channel geometrical characteristics but with important changes in the channel spins [16,17]. Third, a given composite system can be populated by these reactions using different entrance channels, e.g., ^{28}Al formed by the ^{17}O+^{11}B, ^{18}O+^{10}B, and ^{19}F+^{9}Be reactions. By varying the entrance channel, it is possible to verify that the Bohr hypothesis of compound-nucleus reactions is satisfied [15].

The paper is organized as follows. The experimental setup is briefly described in Sec. II. Results for the different identified processes are outlined in Sec. III. Discussions and model predictions are presented in Sec. IV. The conclusions are discussed in Sec. V.

II. EXPERIMENTAL SETUP

The measurements were performed using ^{16,17,18}O (22 MeV $\leq E_{\text{lab}} \leq$ 64 MeV) and ^{19}F ($E_{\text{lab}} = 56$ MeV) beams from the University of São Paulo Pelletron accelerator. The targets consisted of self-supporting ^{10}B and ^{11}B foils of areal densities between 30 and 50 μg/cm^2 and ^{9}Be foils of areal density 200 μg/cm^2. Carbon buildup was minimized during the exposure by surrounding the target with a liquid-nitrogen-cooled ring and using a cryogenic pumping system.

0556-2813/94/49(4)/2018(18)/$06.00

The atomic number of charged reaction products and elastically scattered particles was identified using a position-sensitive ionization chamber (PSIC) followed by a large-area solid-state detector [17]. The in-plane angular acceptance of this detector was 6°. In addition, mass identification was achieved using a time-of-flight telescope (TOFT) [17] fixed at $\theta_{\rm lab} = 15°$ on the opposite side relative to the beam direction and composed of a microchannel-plate time (MCP) detector, used in conjunction with another ionization chamber, 1.8 m upstream from the MCP detector. A schematic diagram of the experimental setup is presented in Ref. [17] and Fig. 1(a). The ΔE and time resolutions ($\delta\Delta E/\Delta E < 6\%$ and $\Delta t \approx 700$ ps) were sufficient to provide a unit mass and charge resolution. Absolute cross sections, as well as the amount of carbon and oxygen contamination present in the target, were determined by comparing the elastic-scattering cross sections to optical-model predictions.

A description of the angular and energy range covered by this work is presented in Table I. As indicated in Table I(b), coincidence data between the fragments detected by the TOFT fixed at $\theta_1 = -15°$ and the PSIC were obtained for the ^{18}O+^{10}B and ^{17}O+^{11}B reactions at $E_{\rm lab} = 53$ MeV. The coincidence kinematics for ^{18}O+^{10}B reaction, typical of the reactions studied, is indicated in Fig. 1(b). As evident from this figure, for the coincidence measurements, the PSIC scanned a sufficiently wide angular region θ_2 to cover the complete Q-value range for all possible binary exit channels.

III. EXPERIMENTAL RESULTS

A. Elastic scattering

The experimental elastic-scattering angular distributions, presented in Figs. 2 and 3, display a general behavior of oscillatory decreasing cross section with angle and a smooth back-angle enhancement. The origin of the back-angle enhancement and its energy dependence deserved special attention.

There are several plausible explanations for the en-

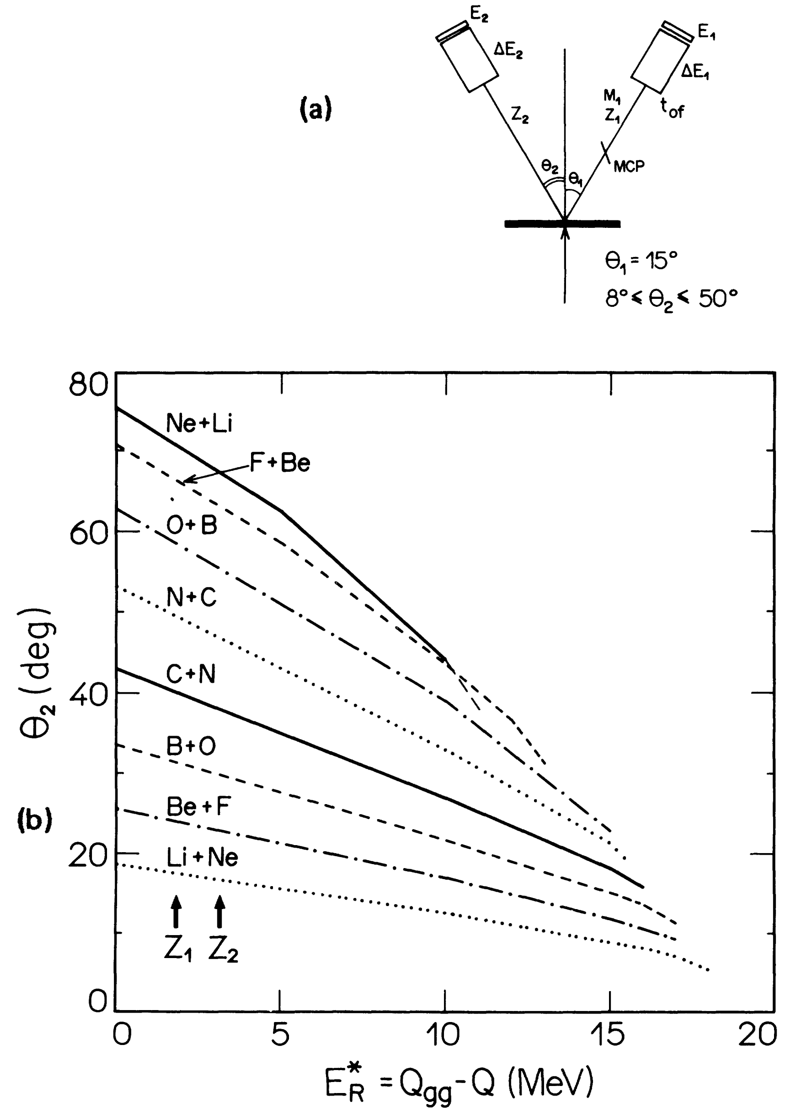

FIG. 1. (a) Experimental setup used for the kinematical coincidence measurements. The angle θ_1 of the TOFT was fixed at $-15°$ and the θ_2 of the PSIC varied from 8° to 50° for the coincidence measurements. (b) Kinematics of the binary products as a function of the mutual excitation energies for the ^{18}O+^{10}B system at 53 MeV.

hanced yields observed at large angles. These yields have been variously attributed to elastic cluster transfer [18], to the coupling of important reactions channels [19], or to compound-elastic processes [16,17]. Here we explore this latter possibility.

The statistical-model code STATIS [20], was used to estimate the contribution of the compound-elastic (CE) processes. The schematic nature of this calculation needs to be emphasized. It is known that variations of the level density and spin-cutoff parameters can induce large changes in Hauser-Feshbach cross sections [21]. For realistic calculations, all of the important decay channels for the relevant partial waves need to be considered.

In principle, the compound-elastic mechanism should be considered within the more general framework of the binary-fission mechanism, whereas the STATIS calculation only includes the neutron, proton, and alpha-particle evaporation channels in addition to the compound-elastic channel. Also, in the case of the compound-elastic channel, as well as for the emission of other complex fragments, the absolute cross-section magnitude is strongly dependent on the angular momentum distribution assumed for the compound nucleus [21].

Although the above caveats suggest that a detailed description of the experimental results cannot be expected, the STATIS calculations are still useful to gauge the likely importance of the compound-elastic mechanism. These studies can also help in establishing the angular dependence of the process since full spin-weighted calculations are done. In contrast, the fission transition-state model, discussed later in this paper, only determines the total decay probabilities to the final channels. The transmission coefficients for STATIS, including the compound-elastic decay channel, were parametrized in terms of Fermi functions adjusted to reproduce fusion and reaction cross sections, respectively. The optical-model (OM) parameters, indicated in Table II, were obtained from individual χ^2 fits to the elastic-scattering distributions assuming an incoherent sum of direct and compound-elastic amplitudes, with $\sigma_{\text{elastic}} = \sigma_{\text{OM}} + \sigma_{\text{CE}}$.

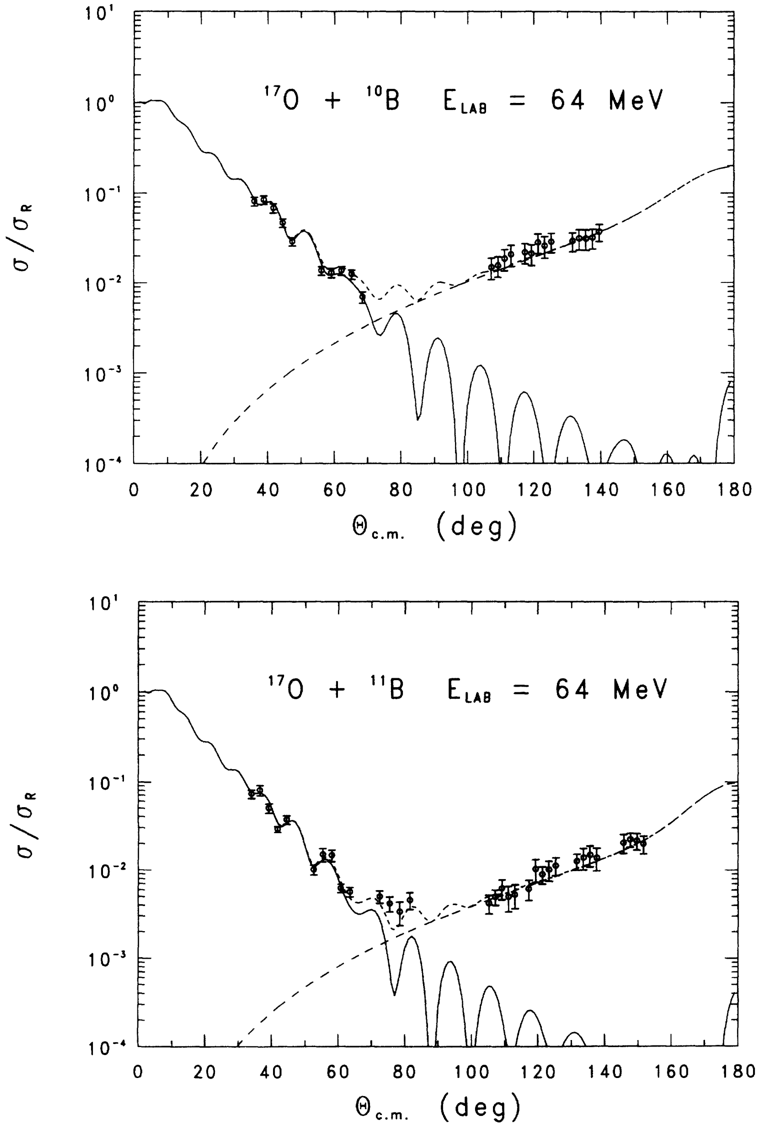

FIG. 2. Elastic-scattering angular distributions $\sigma/\sigma_{\text{Ruth}}$ for the $^{17}\text{O}+^{10,11}\text{B}$ systems at the highest energy. The solid curve represents a fit of the data at forward angles to the optical model (PTOLEMY). The dashed curve represents fit to the statistical model (STATIS), and the dotted curve represents the incoherent sum of both fits.

The forward-angle data were fitted by OM predictions using the computer code PTOLEMY [22].

Fits presented in Figs. 2 and 3 indicate that the CE contributions account very well for the structureless behavior observed in the experimental back-angle data. These results indicate that the CE process may fully account for the observed large-angle yields.

B. Fusion components

One of the difficulties that is frequently encountered while analyzing evaporation-residue yields of light heavy-ion fusion reactions is that certain elements can be produced by multiple-reaction mechanisms. As an example, the incomplete-fusion mechanism occurs when nucleon or light-fragment emission takes place early in the reaction process, thus leading to a composite system whose linear momentum is different from that of the projectile. This incomplete-fusion system might subsequently decay by light-particle emission to produce the same elements formed by the complete-fusion process [16,23–25]. As a second example, a given element might be produced as the end product of a chain of light-particle evaporations or, alternatively, it might be produced directly through the binary decay of the compound nucleus or even through a direct transfer process.

To help resolve these ambiguities, it is useful to analyze the velocity spectra converted to the center-of-mass frame. Since the shapes of velocity spectra for evaporation residues can be satisfactorily reproduced by statistical-model calculations [23–25], channels in which evaporation residues and other components are simultaneously present can be unfolded by subtracting from the experimental spectra the evaporation-residue yield predicted by these calculations.

In the present analysis, reaction products with $Z = 12$, 11, 10, and 9 were identified as being essentially evaporation residues (ER's) resulting from a complete-fusion process. On the other hand, the elements with $Z = 3$, 4,

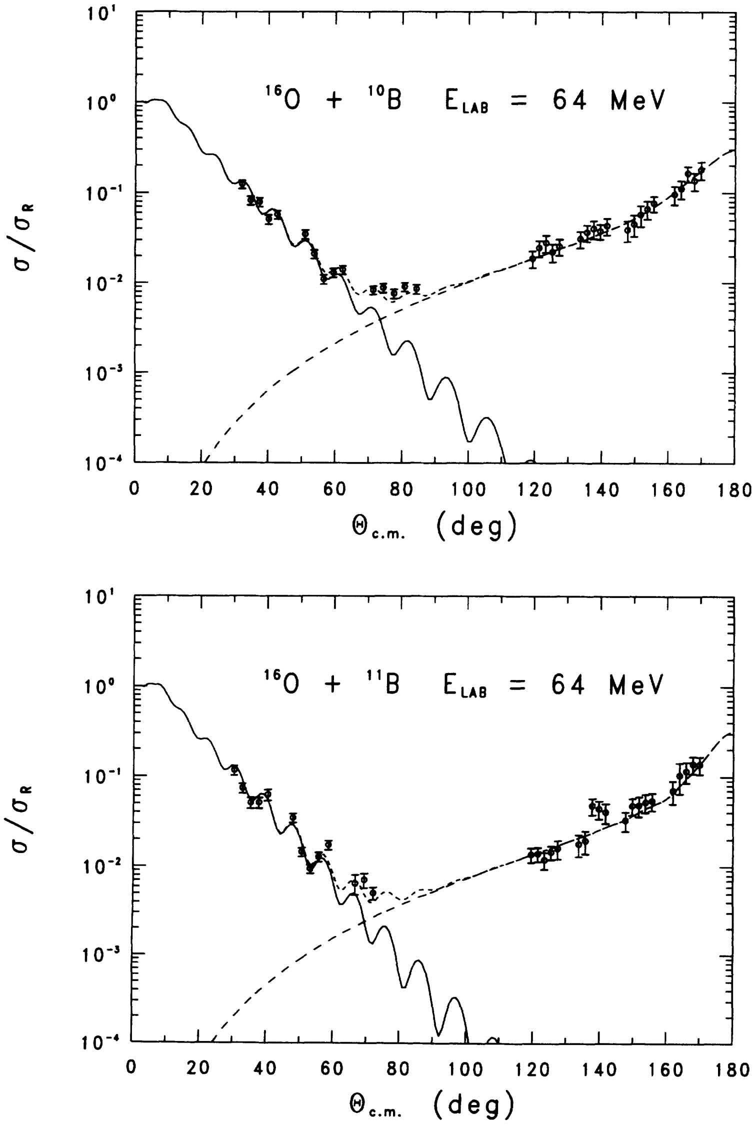

FIG. 3. Same as Fig. 2 for the $^{16}O+^{10,11}B$ systems.

TABLE I. (a) Angular and energy ranges covered in this paper for the inclusive measurements. The angle $\theta_{\mathrm{lab}}(\mathrm{deg})_{\mathrm{PSIC}}$ represents the value of the central position. In fact five angles, separated by 1°, are measured simultaneously. (b) Angular ranges converged for the coincidence measurements for the $^{18}O+^{11}B$ and $^{17}O+^{11}B$ reactions at 53 MeV.

(a)

$^{16}O+^{10,11}B$		$^{17}O+^{10}B$	
E_{lab} (MeV)	$\theta_{\mathrm{lab}}(\mathrm{deg})_{\mathrm{PSIC}}$	E_{lab} (MeV)	$\theta_{\mathrm{lab}}(\mathrm{deg})_{\mathrm{PSIC}}$
22	12	22	12
28	12	28	12
34	12	34	12
42	8,15,22,29,35	42	10,18,26,35
49		49	12
56	8,15,22,29,35	56	12
64	8,15,22,29	64	8,15,22,29,35

$^{17}O+^{11}B$		$^{18}O+^{10,11}B$	
E_{lab} (MeV)	θ_{lab} $(\mathrm{deg})_{\mathrm{PSIC}}$	E_{lab} (MeV)	$\theta_{\mathrm{lab}}(\mathrm{deg})_{\mathrm{PSIC}}$
22	12	22	12
28	12	28	12
34	12	32	8,15,22,29,35
42	8,15,22,29,35	40	8,15,22,29,35
49	12	48	8,15,22,29,35
56	8,15,22,29,35	55	9,17,25
64	8,15,22,29,35	63	8,15,22,29

$^{19}F+^{9}Be$

E_{lab} (MeV)	$\theta_{\mathrm{lab}}(\mathrm{deg})_{\mathrm{PSIC}}$
56	9,17,26,35

(b)

Reaction	$\theta_{\mathrm{lab}}(\mathrm{deg})_{\mathrm{PSIC}}$
$^{18}O+^{10}B$	12.0,18.0,24.0,27.0,36.0 65.0,66.0,66.5,67.5,68.5,69.5,70.5
$^{17}O+^{11}B$	18.0,26.0

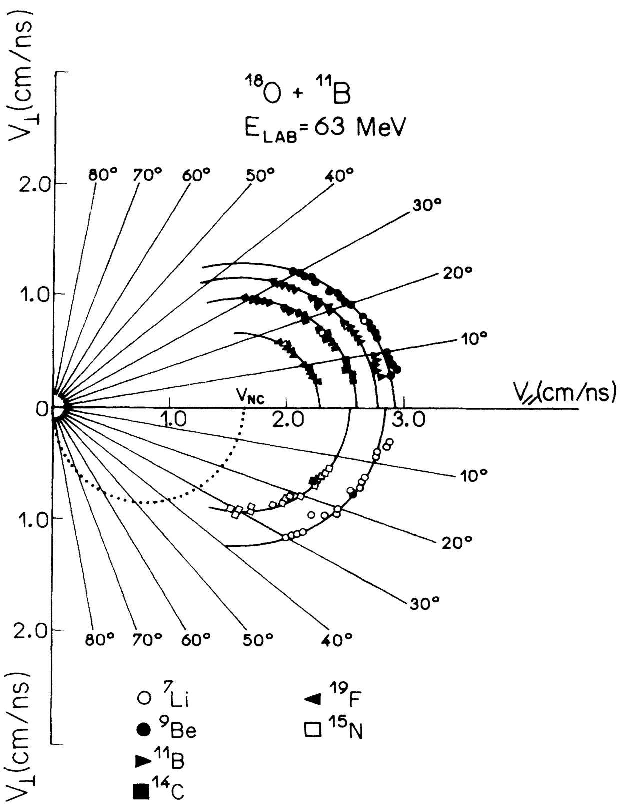

FIG. 4. Typical velocity plot for the "nonevaporation-residue" components of the $^{18}O+^{11}B$ reaction at 63 MeV. The circles, centered at the center-of-mass velocity, describe the loci for products with constant Q values.

5, and 6 were identified as resulting from a binary-decay mechanism. These results are supported by statistical-model predictions and by the velocity angular distributions (see Fig. 4). In the intermediate region, e.g., $Z = 7$ and 8, there is evidence of competition between evaporation residues, binary, and more direct reaction components with relative intensities of the processes varying with angle and bombarding energy.

The unfolding procedure is illustrated in Fig. 5(a) for the ^{15}N products from the $^{18}O+^{10}B$ reaction. The hatched region is a result of the subtraction of the estimated evaporation-residues contribution (dashed histogram obtained by scaling the calculated distribution) from the experimental ^{15}N spectrum. It is interesting to note that the resulting ^{15}N spectrum is very similar in shape and magnitude to the $^{11}B(^{18}O,^{15}N)$ spectrum for which no evaporation-residue contribution is predicted, as seen in Fig. 5(b). The validity of this procedure is supported by the good representation achieved by the statistical-model calculations in describing the shape of the resulting ER angular distributions (see Fig. 6), as well as by the regular behavior of the velocity distributions of the resulting non-ER yields. These yields will be discussed further in the following section. Details on the unfolding procedure are presented in Refs. [16] and [17]. The contribution from the small amount of ^{12}C and ^{16}O target contamination, as determined by the low-energy elastic-scattering data, has been subtracted based on A, Z, and E distributions estimated from Monte Carlo Hauser-Feshbach calculations (using the LILITA code) [24] and normalized to values for the ER cross sections found in the literature for the $^{16,17,18}O+^{12}C$, ^{16}O reactions.

Values for evaporation-residue differential cross sections were obtained for the $^{16,17,18}O+^{10,11}B$ reactions and $^{19}F+^{9}Be$ reaction. Typical angular distributions for individual elements are presented in Fig. 6. The curves indicate the LILITA prediction normalized to the data. Total cross sections $\sigma_F(E)$ for evaporation-residue production are determined by first finding the functional expression $g(\theta)$ that could accurately reproduce the experimental distributions $g(\theta) \approx \sum_z d\sigma_z/d\Omega_{\mathrm{exp}}$ and could be extrapolated to zero degrees and to large angles [17]. The area under this function was then determined to obtain the total fusion cross section, with

$$\sigma_F(E) = \int_0^{\theta_{\max}} 2\pi \, \sin\theta_L \left\{ \sum_Z \left(\frac{d\sigma_Z}{d\Omega} \right) \right\} d\theta_L \, . \tag{1}$$

Uncertainties in the total cross sections, estimated to

TABLE II. Optical-model parameters for the ^{16,17,18}O+^{10,11}B reactions.

$E_{\rm lab}$ (MeV)	V_0 (MeV)	r_r (fm)	a_r (fm)	W_0 (fm)	r_i (fm)	a_I (fm)
^{16}O+^{10}B						
42	100	1.15	0.64	4.2	1.80	0.57
56	100	1.15	0.64	7.2	1.74	0.70
64	100	1.21	0.64	15.0	1.50	0.76
^{16}O+^{11}B						
42	100	1.15	0.64	4.2	1.66	0.74
56	100	1.15	0.64	7.2	1.80	0.72
64	100	1.21	0.64	16.2	1.47	0.77
^{17}O+^{11}B						
42	100	1.15	0.64	7.0	1.64	0.70
64	100	1.21	0.64	8.4	1.65	0.70
^{17}O+^{11}B						
42	100	1.15	0.64	7.2	1.65	0.73
56	100	1.15	0.64	6.4	1.83	0.70
64	100	1.21	0.64	8.4	1.66	0.75
^{18}O+^{10}B						
32	100	1.15	0.64	6.7	1.52	0.43
40	100	1.15	0.64	8.5	1.53	0.70
48	100	1.15	0.64	7.8	1.59	0.78
55	100	1.15	0.64	7.3	1.63	0.76
63	100	1.21	0.64	12.9	1.47	0.72
^{18}O+^{11}B						
32	100	1.13	0.65	8.2	1.46	0.44
40	100	1.15	0.64	7.0	1.63	0.70
48	100	1.15	0.64	7.9	1.60	0.78
55	100	1.15	0.64	7.3	1.63	0.75
63	100	1.21	0.64	11.8	1.50	0.72

be ≈ 10%–15%, reflect counting statistics, extrapolation of the data to zero and large angles, uncertainties in the determination of target thickness and detector solid angle, and errors originating from subtraction of contributions from contaminants and binary-reaction processes. Differential cross sections for complete fusion are presented in Figs. 7–9. The curves are the predictions of the code LILITA [24], scaled to the data. Good overall agreement between the calculated and experimental results is observed.

Experimental excitation functions are presented in Fig. 10. Fits to the evaporation-residue excitation function

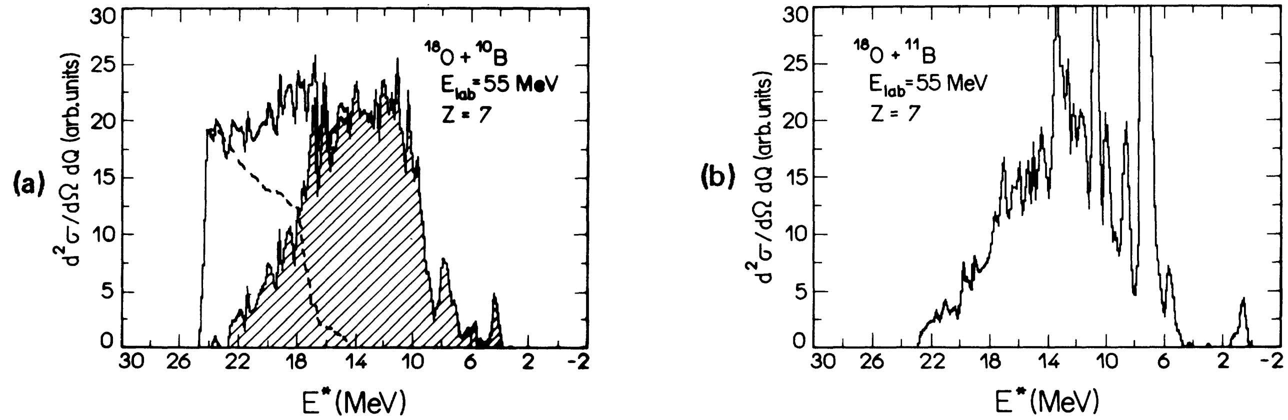

FIG. 5. Unfolding of the ^{10}B(^{18}O,^{15}N) Q-value-converted spectrum assuming a ^{15}N+^{13}C binary channel. (a) The solid line corresponds to the raw data, and the dashed spectrum corresponds to the evaporation-residue contributions (calculated using the statistical-model code LILITA); the hatched spectrum corresponds to the resultant subtracted spectrum associated with nonevaporation-residue nitrogen components. (b) The ^{11}B(^{18}O,^{15}N) Q-value spectrum obtained from the raw data. No evaporation residues are predicted or observed in this channel.

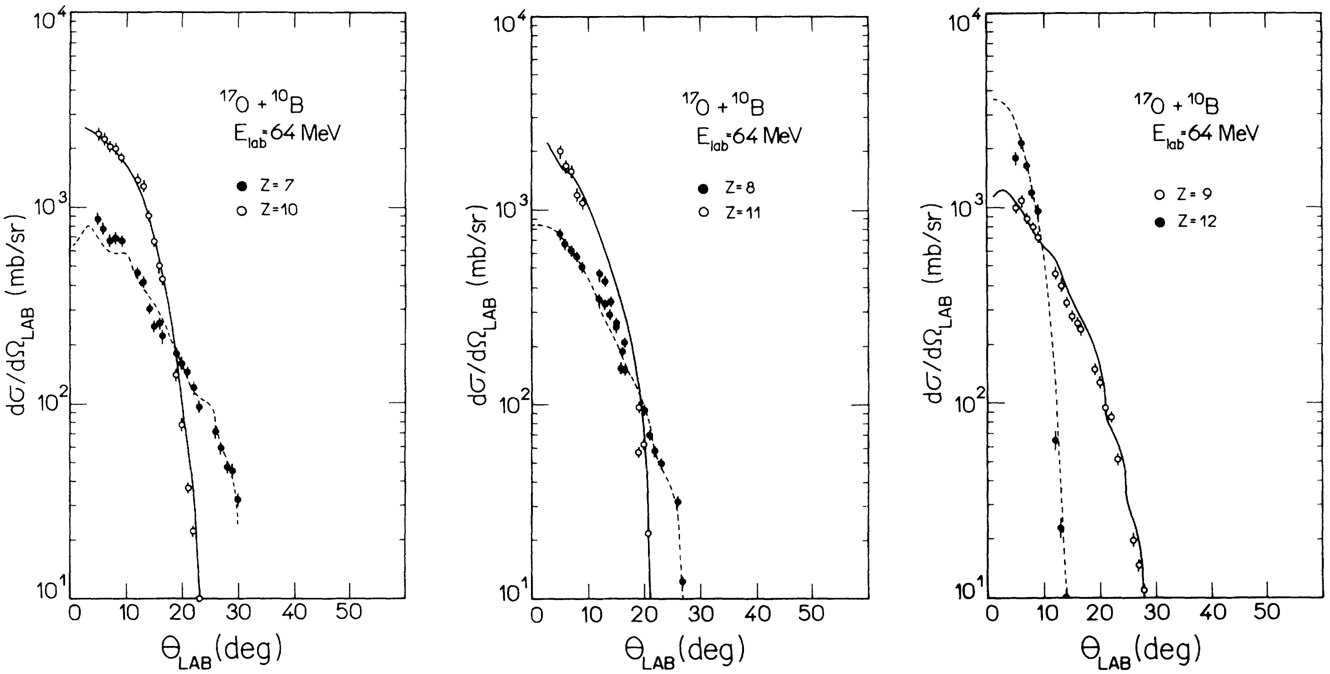

FIG. 6. Comparison between the experimental angular distributions for several evaporation residues (circles) and the Monte Carlo Hauser-Feshbach calculations normalized to the data (LILITA) for the $^{17}O+^{10}B$ reaction at E_{lab} = 64 MeV.

were done with the Glas-Mosel model [26] to determine the fusion barrier height V_B and barrier radius R_B. The experimental V_B and R_B values are listed in Table III. The extracted barrier parameters follow, within the experimental uncertainties, the overall systematics established for this mass region [16].

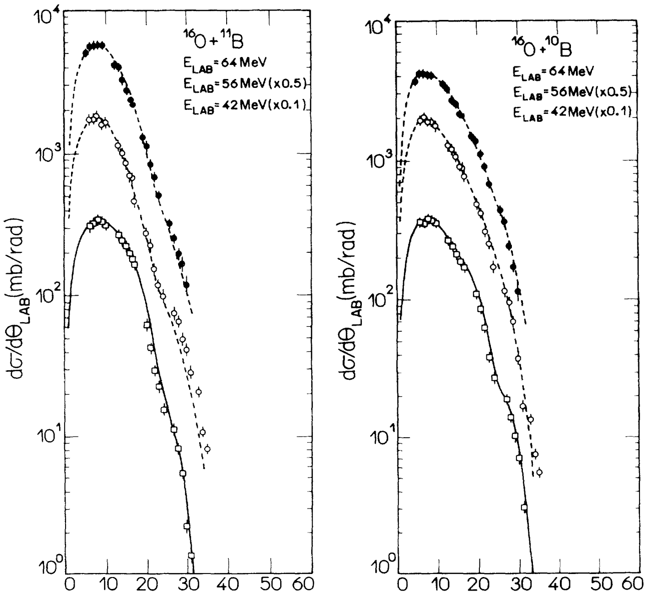

FIG. 7. Experimental angular distributions ($d\sigma/d\theta$) of the $^{16}O+^{10,11}B$ reactions. The curves represent predictions of the LILITA code normalized to the data.

IV. BINARY-REACTION CHANNELS

A. Inclusive cross sections

After extracting the ER yields resulting from light-particle evaporation from the compound nucleus, there remains a second reaction component that also appears to result from compound-nucleus decay. This origin can

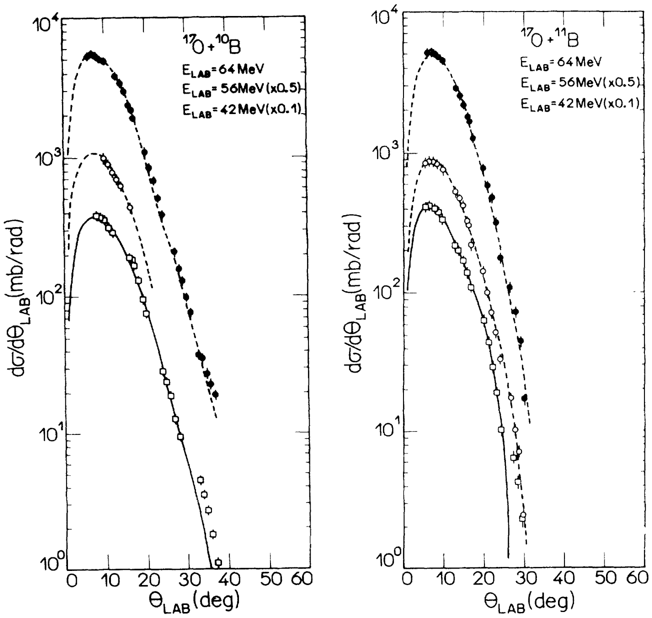

FIG. 8. Same as Fig. 7 for the $^{17}O+^{10,11}B$ reactions.

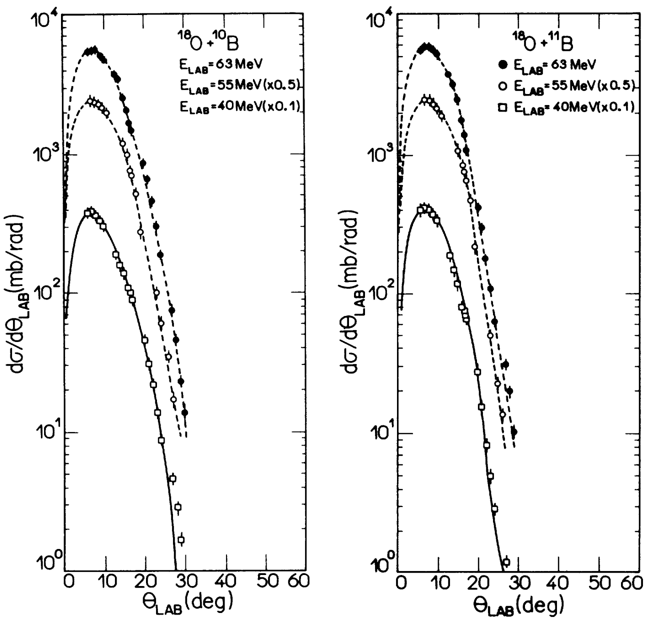

FIG. 9. Same as Fig. 7 for the ^{18}O+^{10,11}B reactions.

be deduced by noting that the contours of constant invariant differential cross sections for these yields as functions of their longitudinal and transverse velocity components $v_{\parallel} \times v_{\perp}$, as shown in Fig. 4, are centered at the velocity of the center of mass. Assuming a binary-decay process, as will be confirmed by the coincidence measurement, it is possible to establish from these data channel-dependent values for the most probable total kinetic energies ⟨TKE⟩ and corresponding Q values, with the most probable mass value for each nuclear charge determined by the TOFT data.

Contributions from binary-reaction processes were clearly identified in the lithium, beryllium, boron, carbon, oxygen, and fluorine channels. Their angular distributions are presented in Figs. 11–13. The anisotropy of these angular distributions about $\theta_{\text{c.m.}} = 90°$ may be associated with the "lifetime" τ of the intermediate nuclear configuration by using the Regge-pole model [27]. The lifetime $\tau = \alpha/\omega$ is related to the observed "life angle" α and the intermediate nucleus angular velocity ω. To determine these quantities, the experimental angular distributions were fitted by the expression

$$\frac{d\sigma}{d\Omega} = \frac{C}{\sin\theta_{\text{c.m.}}}\left[\exp\left(-\frac{\theta_{\text{c.m.}}}{\alpha}\right) + \exp\left(-\frac{2\pi-\theta_{\text{c.m.}}}{\alpha}\right)\right]. \tag{2}$$

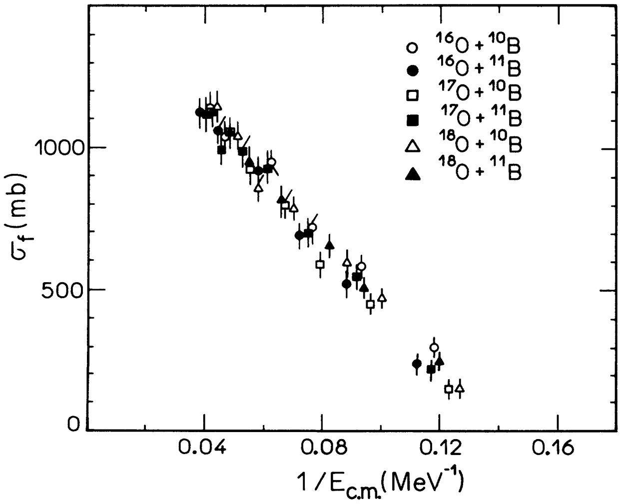

FIG. 10. Experimental fusion cross sections plotted vs $1/E_{\text{c.m.}}$ for the ^{16,17,18}O+^{10,11}B systems.

TABLE III. Experimental values for fusion barriers height (V_B) and (R_B) obtained in the present work and from Ref. [25].

	Present work		Reference [25]	
System	V_B (MeV)	R_B (fm)	V_B (MeV)	R_B (fm)
^{16}O+^{10}B	6.8±0.2	7.0±0.1	6.7	7.0
^{16}O+^{11}B	7.7±0.2	7.1±0.1	7.7	7.1
^{17}O+^{10}B	7.2±0.2	7.0±0.1	6.7	7.1
^{17}O+^{11}B	7.2±0.2	7.1±0.1		
^{18}O+^{10}B	7.1±0.2	7.1±0.1		
^{18}O+^{11}B	7.2±0.2	7.1±0.1		

Values obtained for the life angle α are indicated in Figs. 11–13. Long-lived nuclear configurations ($\tau \geq 2\pi/\omega$), associated with large life angles, present isotropic angular distributions in the reaction plane ($d\sigma/d\Omega \propto 1/\sin\theta$). This was found for the C, B, Be, and Li products, associated with targetlike particles, for all of the systems and energies investigated. Alternatively, the N, O, and F products, associated with projectilelike particles, present forward-peaked angular distributions with different $25° \leq \alpha \leq 45°$, suggesting that a more peripheral reaction mechanism dominates the small-angle yields in these channels.

Reaction anisotropies can also be deduced for individual masses identified by the TOFT fixed at $\theta_{\text{lab}} = 15°$ as shown in Fig. 14. Assuming binary decays, the angular distributions for the partners x-y ≡C-N, O-B, F-Be, Ne-Li must have similar behavior, that is, if they originate from the same long-lived process, $d\sigma(x,\theta) = d\sigma(y,(\pi-\theta))$. The absence of this symmetry in some of the C-N cases, as illustrated in Figs. 11–13, again suggests a significant direct-reaction component dominating the forward-angle nitrogen distributions.

A general feature to the non-ER energy spectra, as seen, for example, in Fig. 5, is the superposition of narrow peaks on the otherwise bell-shaped distributions. These peaks are associated with the mutual excitation of particle-bound states (or relatively long-lived states) of both projectilelike and targetlike reaction fragments. This fact further supports the binary nature of the process as this structure will be attenuated for more complicated processes involving three or more particles. It is interesting to note that the structure persists to very

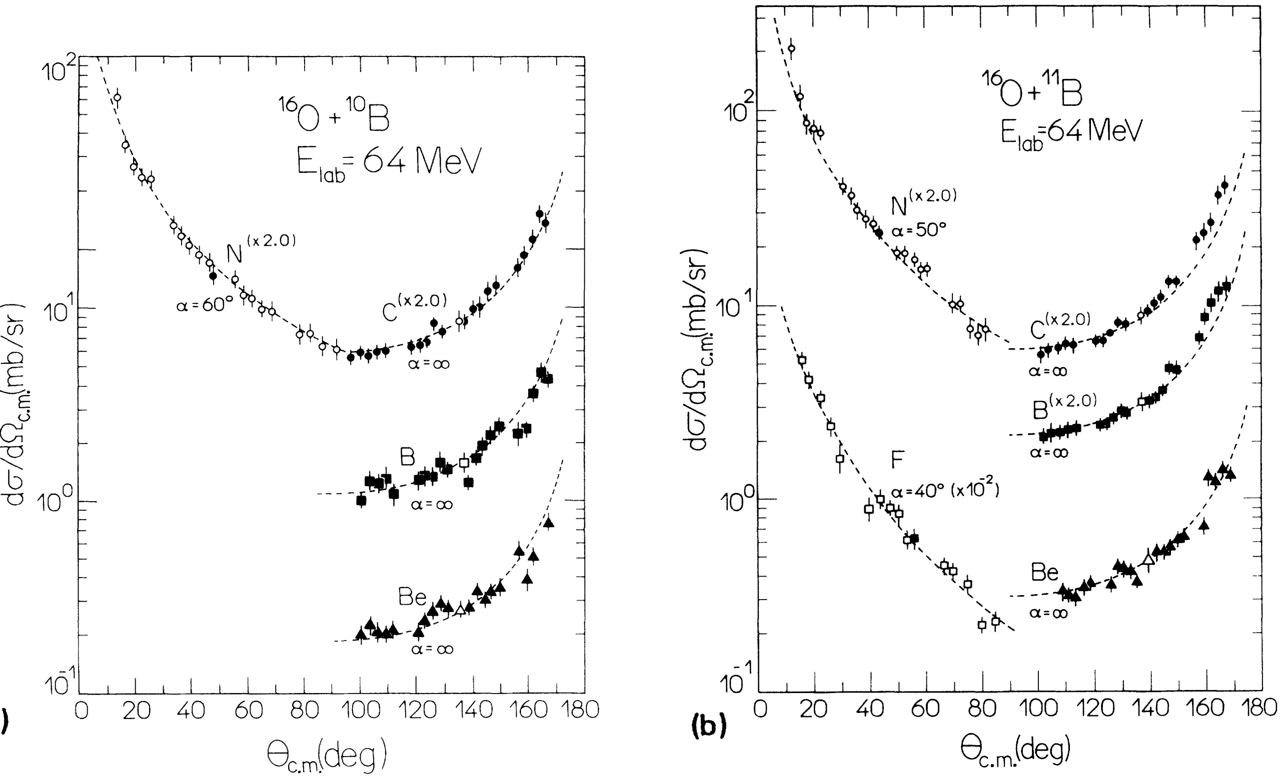

FIG. 11. Angular distribution of "nonevaporation" components for (a) $^{16}O+^{10}B$ and (b) $^{16}O+^{11}B$ reactions. The dashed curves represent fits by Eq. (2). Experimental values for the life angle α are indicated in each case. Angular distributions for targetlike particles are presented at backward angles.

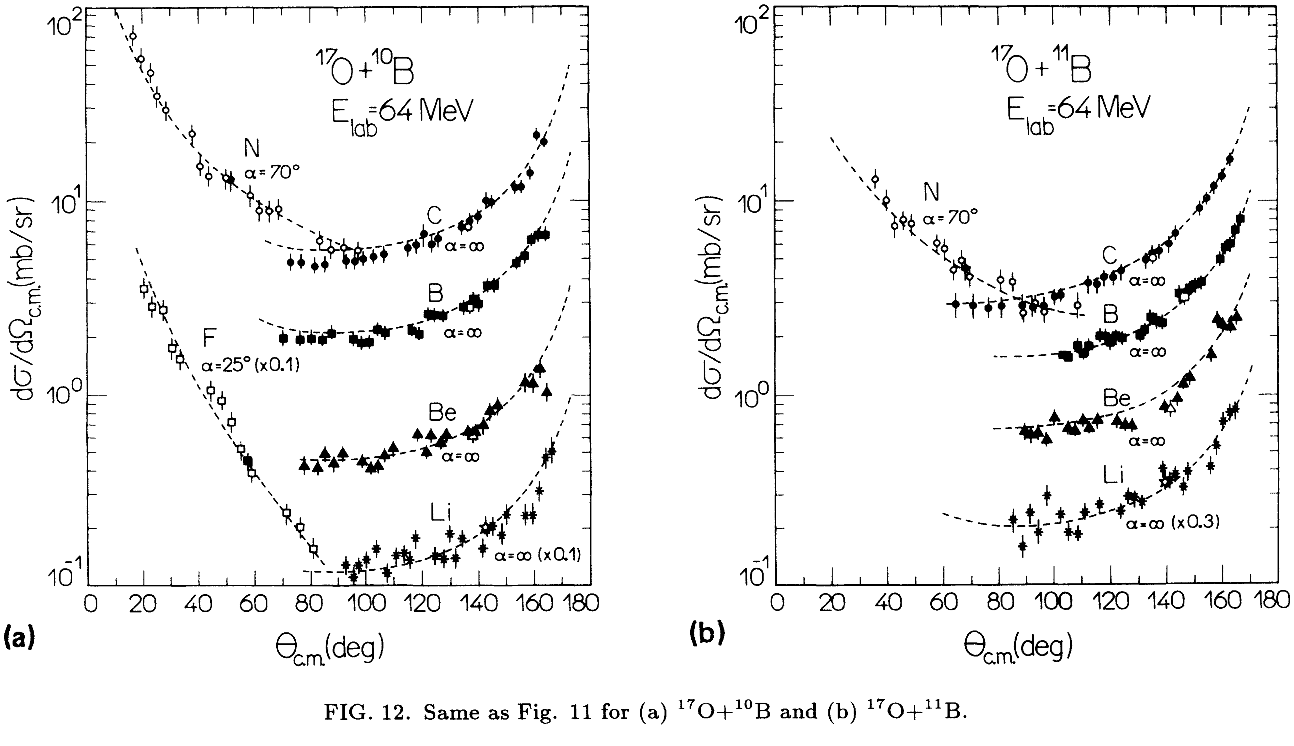

FIG. 12. Same as Fig. 11 for (a) $^{17}O+^{10}B$ and (b) $^{17}O+^{11}B$.

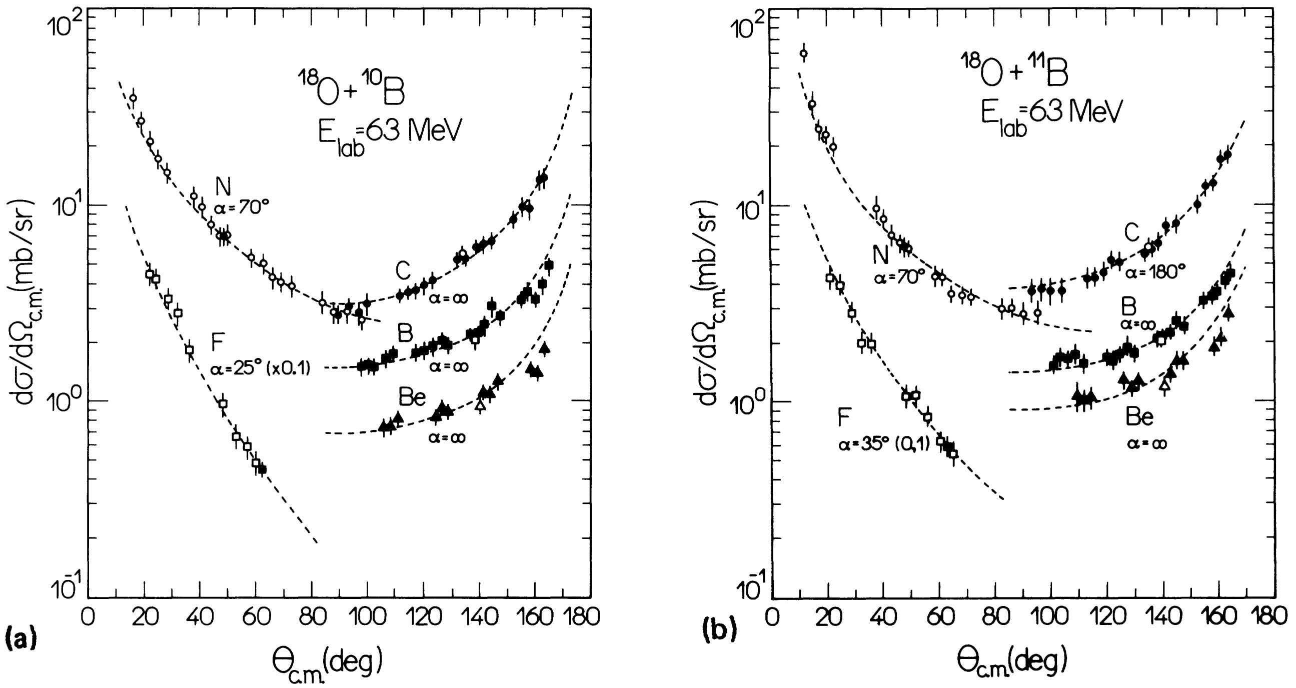

FIG. 13. Same as Fig. 11 for (a) $^{18}O+^{10}B$ and (b) $^{18}O+^{11}B$.

negative Q values, indicating a high selectivity in the breakup process.

Although the singles data offer compelling evidence of significant binary-reaction yields, the experimental confirmation of such yields requires the detection of both fragments in coincidence. In the next section, we discuss such coincidence measurements.

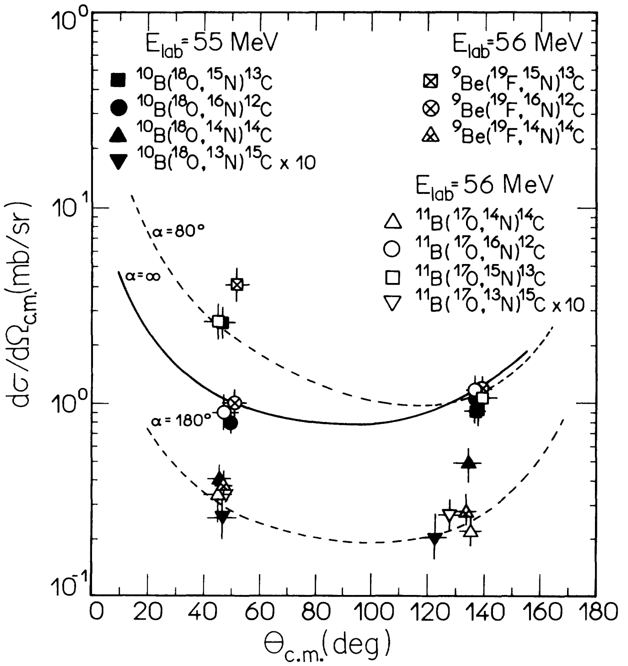

FIG. 14. Differential cross sections for some binary reaction products identified in A and Z. Same as Fig. 7 for the $^{17}O+^{10,11}B$ reactions.

B. Coincidence measurements

Coincidence data between the fragments detected by the TOFT $(d\sigma/d\Omega)(Z_1,A_1,\theta_1)$ and the PSIC $(d\sigma/d\Omega)(Z_2,\theta_2)$ were obtained for the $^{18}O+^{10}B$ reaction and $^{17}O+^{11}B$ reaction at 53 MeV (see Fig. 15). This latter detector covered a wide angular region $8° < \theta_2 < 50°$ and had good efficiency for detecting the recoil fragments associated with the particles identified in the TOFT.

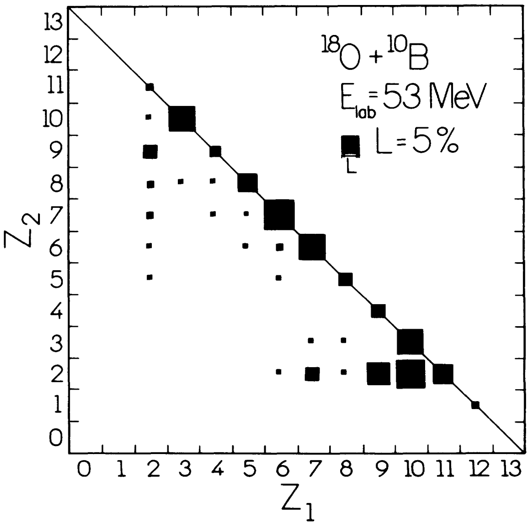

FIG. 15. Typical coincidence matrix Z_1 (TOFT at 16°) vs Z_2 (PSIC at θ_2 integrated over the angular range $8° < \theta_2 < 50°$) for the $^{18}O+^{10}B$ reaction at E_{lab} = 53 MeV. The size of the square is linearly proportional to the relative intensity of the pair.

The angular region covered by the PSIC was sufficient to scan the complete Q-value spectrum of the fully energy-damped binary products (see Fig. 1(b)). To establish the binary-reaction nature of the coincidence yields, energy spectra $(d^3\sigma/d\Omega_1 d\Omega_2 dQ)$ are generated for specific reaction pairs and compared to the corresponding singles spectra of $(d^2\sigma/d\Omega_1 dQ)$ obtained with the 5° TOFT. The results, as well as similar results for the other reactions studied, indicate the dominance of binary reaction products for those yields that are not associated with the ER mechanism.

A typical coincidence matrix for the binary products is presented in Fig. 15. The sizes of the squares are proportional linearly to the differential cross sections $(d^3\sigma/d\Omega_1 d\Omega_2 dQ)$. The $Z_1 + Z_2 = Z_{\text{CN}}$ line represents the loci for binary products. The effect of secondary light-particle emission, which results in the population of channels with $Z_1 + Z_2 < Z_{\text{CN}}$, is small. It is only for the heaviest fragments observed in the TOFT detector (corresponding to large Z_1) where this effect, associated to the contributions of evaporation residues, is found to be significant. It should be noted that the binary nature of the reaction products has also been verified in terms of the mass of the fragment using the mass identification of the TOFT in conjunction with the position information of the PSIC and binary-reaction kinematics.

C. Properties of the binary products

The forward-peaked angular distributions and corresponding small life angles α of the $Z \geq 7$ elements reveal a major contribution of direct processes. However, in the case of $Z \leq 6$ elements, the isotropic angular distributions point toward a process in which a long-lived intermediate nuclear configuration is formed. Two competing processes, deep-inelastic orbiting and compound nuclear fusion, may produce such yields.

1. TKE of the binary-reaction component

Experimental values for the total kinetic energy ⟨TKE⟩ in the exit channels as a function of bombarding energy are shown in Fig. 16. The values are obtained under the assumptions that arise from binary processes using the most probable mass values identified by the TOFT. For the fully energy-damped processes, the TKE is expected to peak at a value related to the potential energy of the system at scission, with

$$\langle \text{TKE} \rangle = V_N + V_C + \left(\frac{\hbar^2}{2\theta}\right)[l(l+1)] \,, \qquad (3)$$

where V_N describes the nuclear interaction potential, V_C the Coulomb interaction, and the third term describes the centrifugal energy. The curve in Fig. 16 describes the predictions based on the nuclear shape extracted at the saddle-point configuration (see Sec. V A) for a fissioning compound nucleus.

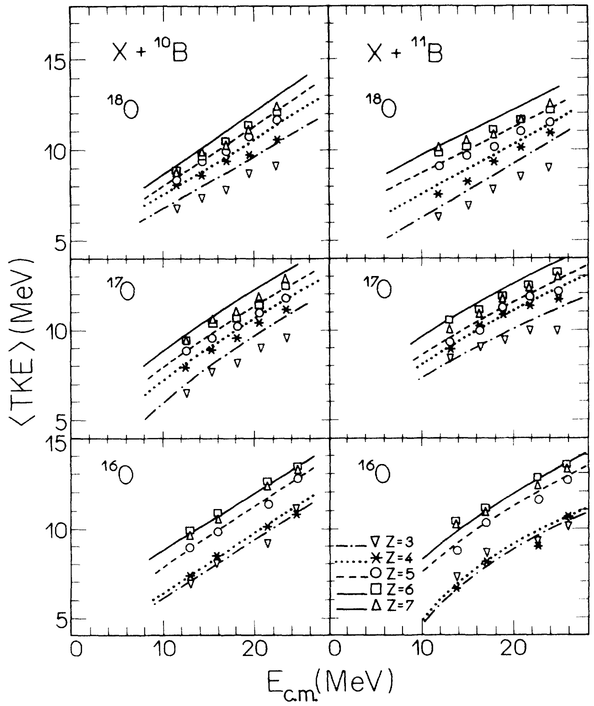

FIG. 16. Experimental values for the total kinetic energy ⟨TKE⟩ for the ^{16,17,18}O+^{10,11}B systems. Curves describe predicted values on the basis of Eq. (3) (for details see the text).

2. Entrance-channel dependence

Recent measurements have demonstrated the presence of strongly energy-damped binary processes in heavy-ion reactions [3–10,28–32]. In the case of systems with $A_1 + A_2 \geq 40$, a controversy has developed concerning the reaction dynamics leading to the emission of these complex fragments. Two competing processes, deep-inelastic orbiting and compound-nucleus (CN) fusion followed by fission, have been suggested as possible mechanisms. Both processes lead to totally relaxed reaction products. Therefore the 1/sinθ angular distributions cannot be used as a signature of the process. The main experimental observable that can be used to distinguish between a direct reaction orbiting mechanism and a CN fusion-fission process is the presence or absence of an entrance-channel dependence for the energy-damped yields. The orbiting mechanism, where the colliding nuclei form a complex dinucleus without reaching the more compact configuration of an equilibrated compound nucleus, is expected to be strongly dependent on the specific nature of the entrance channel. The fusion-fission process, alternatively, assumes the formation of an equilibrated CN, where the only memory of the entrance channel is through the conserved quantities. This criterion, independent of calculation uncertainties and based on the Bohr hypothesis, is a fundamental characteristic of compound-nucleus processes.

This criterion has been used in the case of the reactions

$$\begin{array}{llll} {}^{19}\mathrm{F} + {}^{9}\mathrm{Be} \searrow & & \nearrow \mathrm{C}+\mathrm{N} \\ {}^{18}\mathrm{O} + {}^{10}\mathrm{B} \rightarrow & {}^{28}\mathrm{Al} & \rightarrow \mathrm{B}+\mathrm{O} \\ {}^{17}\mathrm{O} + {}^{11}\mathrm{B} \nearrow & & \searrow \mathrm{Be}+\mathrm{F} \\ & & \searrow \mathrm{Li}+\mathrm{Be} \end{array}$$

and

$$\begin{array}{llll} {}^{17}\mathrm{O} + {}^{10}\mathrm{B} \searrow & & \nearrow \mathrm{C}+\mathrm{N} \\ {}^{16}\mathrm{O} + {}^{11}\mathrm{B} \rightarrow & {}^{27}\mathrm{Al} & \rightarrow \mathrm{B}+\mathrm{O} \\ & & \searrow \mathrm{Be}+\mathrm{F} \\ & & \searrow \mathrm{Li}+\mathrm{Be} \end{array}$$

A quantitative comparison can be made by calculating the excitation functions for the angle-integrated cross sections (assuming a $1/\sin\theta$ dependence) of several products as a function of the compound-nucleus excitation energy (E^*_{CN}). This comparison is shown in Fig. 17 and indicates that all of the excitation functions for a given compound nucleus (^{28}Al) leading to the same decay channel are identical, independent of entrance channels. A similar conclusion is reached by comparing the ratio of yields for different exit channels as a function of the excitation energy of the emerging fragments. Figure 18 presents the ratio $R = \sigma_{\mathrm{C}}/\sigma_{\mathrm{B}}$ of yield for carbon products (σ_{C}) compared to the yield for boron (σ_{B}) for three entrance channels populating the same compound nucleus. Although it is not possible, in general, to form a compound nucleus with the same excitation energy and angular momentum distribution using two different entrance channels, those involved in this measurement achieve similar conditions. For the same compound-nucleus excitation energy, the angular momentum distribution inferred from the fusion cross section appears to be similar to within $1\hbar$, assuming a given l diffuseness. The only deviations observed in Fig. 18 are associated with the discrete states at $E^* \leq 7$ MeV, which presumably are populated preferentially by direct processes.

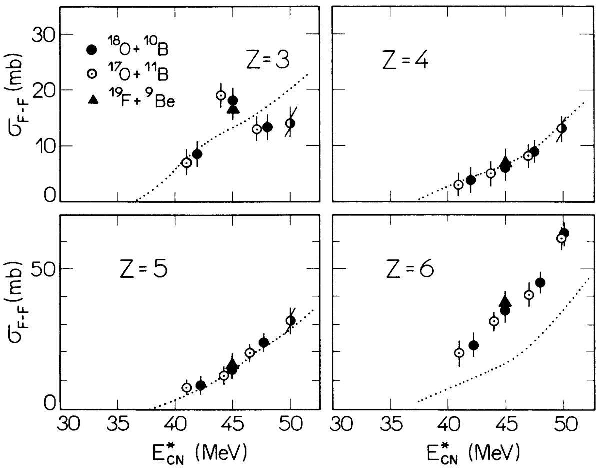

FIG. 17. Excitation function of the strongly energy-damped yields (Z = 3, 4, 5, and 6) from ^{17}O+^{11}B, ^{18}O+^{10}B, and ^{19}F+^{9}Be reactions as a function of the ^{28}Al compound-nucleus excitation energy. The dotted curves represent the "transition-state-model" calculations, considering spin- and mass-asymmetry-dependent saddle-point energies.

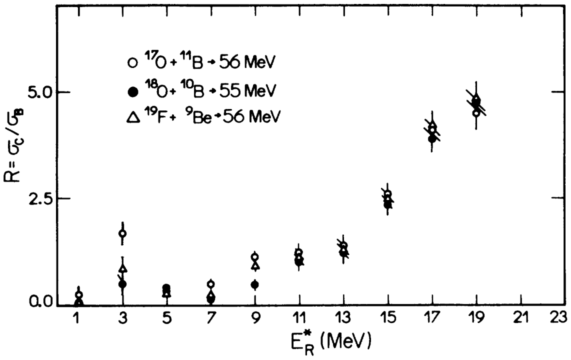

FIG. 18. Ratio of carbon to boron cross section vs the excitation energy of the residual nucleus for different entrance channels forming the ^{28}Al compound nucleus. Fluctuations at very low excitation energies are due to contributions of discrete states populated via direct processes.

V. THEORETICAL DESCRIPTION FOR THE REACTION MECHANISM

A. Fusion-fission calculations

The findings reported above suggest that the strongly energy-damped yields result from a compound-nucleus process. This origin is supported further when a comparison is made between the predictions of statistical fusion-fission calculations and the experimental mass distributions.

Fission cross sections were calculated within the framework of a transition-state model, where the probability of the compound nucleus decaying by the fission mechanism is determined by the available phase space at the saddle-point configuration. Since the details of these calculations are presented in Ref. [30], in the following discussion we will give an overview of the model and concentrate on those aspects that are particularly relevant to the light systems being studied in this work. In these calculations fission is assumed to compete with light-particle emission from the compound nucleus with a branching ratio given by

$$\frac{\Gamma_f}{\Gamma_{\mathrm{tot}}} = \frac{\Gamma_f}{\Gamma_f + \sum_x \Gamma_x}\,, \tag{4}$$

where Γ_{tot} is the total decay width, Γ_f is the fission width, and Γ_x are the partial decay widths for light-particle emission ($x = n$, p, or α). The light-particle widths are calculated in terms of the evaporation-residue level densities, as discussed in Ref. [33]. The fission width Γ_f is obtained from the truncated sum of the partial fission widths to specific channels $\Gamma_f(Z_L, A_L)$, with

$$\Gamma_f = \sum_{A_L=6}^{A_{\rm CN}/2} \sum_{Z_L=A_L/2-2}^{A_L/2+2} \Gamma_f(Z_L, A_L) . \tag{5}$$

The partial widths, specified by the charge Z_L and mass A_L of the lighter fragment, are determined by counting the number of configurations available to mediate the fission decay at the saddle point. Denoting the saddle-point level density as ρ_f, the partial widths are then given by

$$\Gamma_f(Z_L, A_L) = \int_{\epsilon=0}^{\epsilon_{\rm max}} \frac{\rho_f(E - \Delta V - \epsilon, J_{\rm CN})}{2\pi\hbar\rho_{\rm CN} A(E, J_{\rm CN})} T^f_{J_{\rm CN}}(\epsilon) d\epsilon , \tag{6}$$

where

$$E = E^*_{\rm CN} - E_B(Z,A) - E_B^{\rm macro}(Z,A) . \tag{7}$$

E_B is the measured binding energy of the nucleus, and $E_B^{\rm macro}$ is the corresponding macroscopic energy without considering the pairing energy [34]. The spin- and mass-asymmetry-dependent saddle-point energy $V_{\rm saddle}(J_{{\rm CN},\eta})$, included in the ΔV term and determined with respect to the macroscopic energy ground state of the compound nucleus, was found using the double-spheroid approximation discussed in Ref. [30]. $\Delta V_{\rm shell}$, also included in the ΔV term, represents a shell energy correction which was approximated by the sum of the Wigner energy corrections for the two nascent fission fragments [30]. A sharp cutoff approximation is used for the transmission coefficients, with unit transmission for energies above the barrier and blocked fission decay below the barrier. The integration variable ϵ can be envisioned as the radial component of the kinetic energy at the saddle point. It was set an upper limit of $\epsilon_{\rm max} = 20$ MeV.

A Fermi-gas level-density formula was used for both the light-particle evaporation residues and saddle-point configuration with the level-density parameters for the evaporation residues a_x and fission saddle point a_f assumed to be equal, using $a_x = a_f = A/8$ MeV. This is the same level-density assumption that was found to successfully describe the fission behavior in heavier systems with $40 \leq A_{\rm CN} \leq 80$ [30].

An important difference between the present calculation and the corresponding calculations in heavier systems is that a significantly better reproduction of the

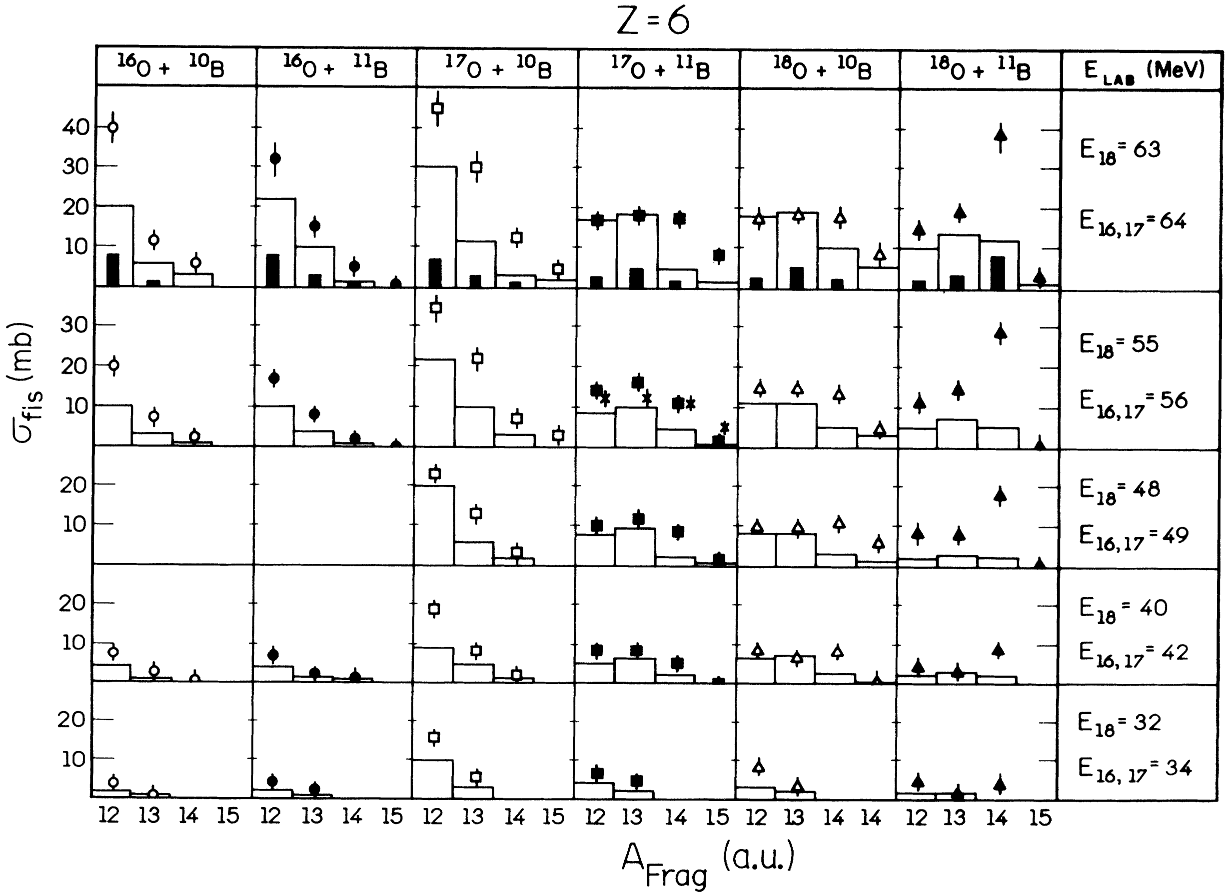

FIG. 19. Experimental fusion-fission cross sections for carbon production compared to the theoretical values predicted by the transition-state model (open histogram). The solid histograms correspond to orbiting calculation for the highest bombarding energy.

light-system results is achieved by increasing the l diffuseness of the fusion partial-wave distribution to $2\hbar$, rather than using the value of $1\hbar$ that was found to give the best overall results in the heavier systems. This change tends to increase the predicted fission yields since it places more cross sections in the higher partial waves that are more likely to lead to fission. It is not possible to claim, however, that these results indicate a characteristic difference between the fusion partial-wave distributions in light and heavier systems. At least two alternative possibilities can be suggested. The first is that the fission barriers are being systematically overpredicted in the lighter systems. Lowering these barriers will increase the predicted fission yield. A second possibility is that taking the ratio of level-density parameters as $a_x/a_f = 1$ is too simplistic. The highly deformed saddle-point configuration is very different from the more spherical shapes expected for the evaporation residues, and it is possible that the level-density parameters will reflect the difference.

The predictions of the transition-state calculations for the fission mass and charge distributions are compared to the experimental results in Figs. 19–22. In making this comparison, it is necessary to correct the calculated fission distributions for the effects of secondary light-particle emissions from the fission fragments. This correction was accomplished by using the binary-channel option of the Monte Carlo evaporation code LILITA [24]. The resulting predictions are found to be satisfactory in reproducing the charge, mass, and bombarding energy dependence of the observed yields, thus supporting the idea that these yields arise from a fission process mediated by a saddle-point transition state.

Using the double-spheroid approximation for the saddle-point energy, it is possible to also estimate the average kinetic energy in the fission channels. This is done by assuming that the saddle- and scission-point configurations are similar and calculating the relative energy of the two spheroids assuming that their centers do not move significantly as the neck snaps [30]. These results are compared with the experimental ⟨TKE⟩ values in Fig. 16 and are found to be in good agreement. This further supports the use of the double-spheroid approximation in describing the fission saddle point.

B. Deep-inelastic orbiting calculations

The equilibrium model for fusion and orbiting developed by Shivakumar *et al.* [31] gives an unified description of fusion and binary decay fragments in terms of an orbiting, dinuclear complex. In a similar way to that of Beck *et al.* [7,8,28], we compare the experimental results for $^{16,17,18}O+^{10,11}B$ with the predicted cross sections from this model for orbiting.

The model uses the Bass parametrization of the nuclear interaction, where the universal function $g(s)$, of the surface separation s, is responsible for the strength of the interaction. According to Shivakumar *et al.*, this strength can be used as a parameter of the model. We have imposed some reasonable limits for $g(s)$ from the

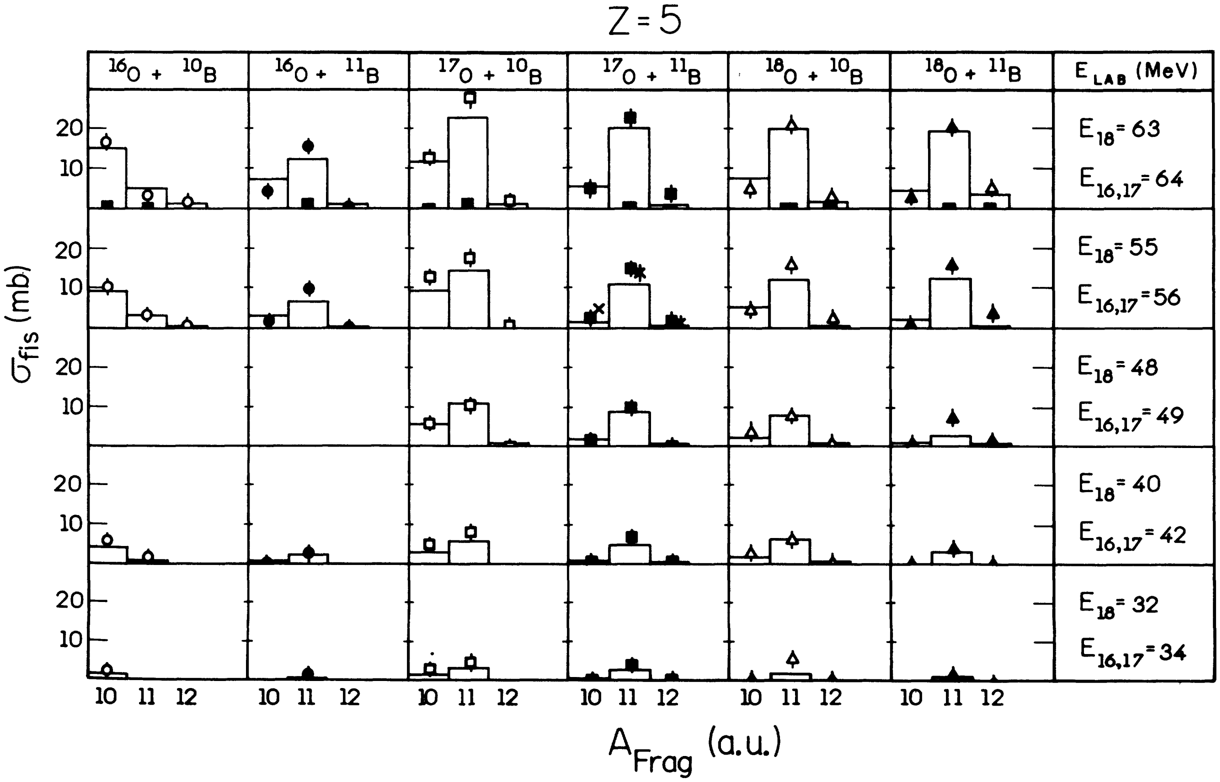

FIG. 20. Same as Fig. 19 for boron.

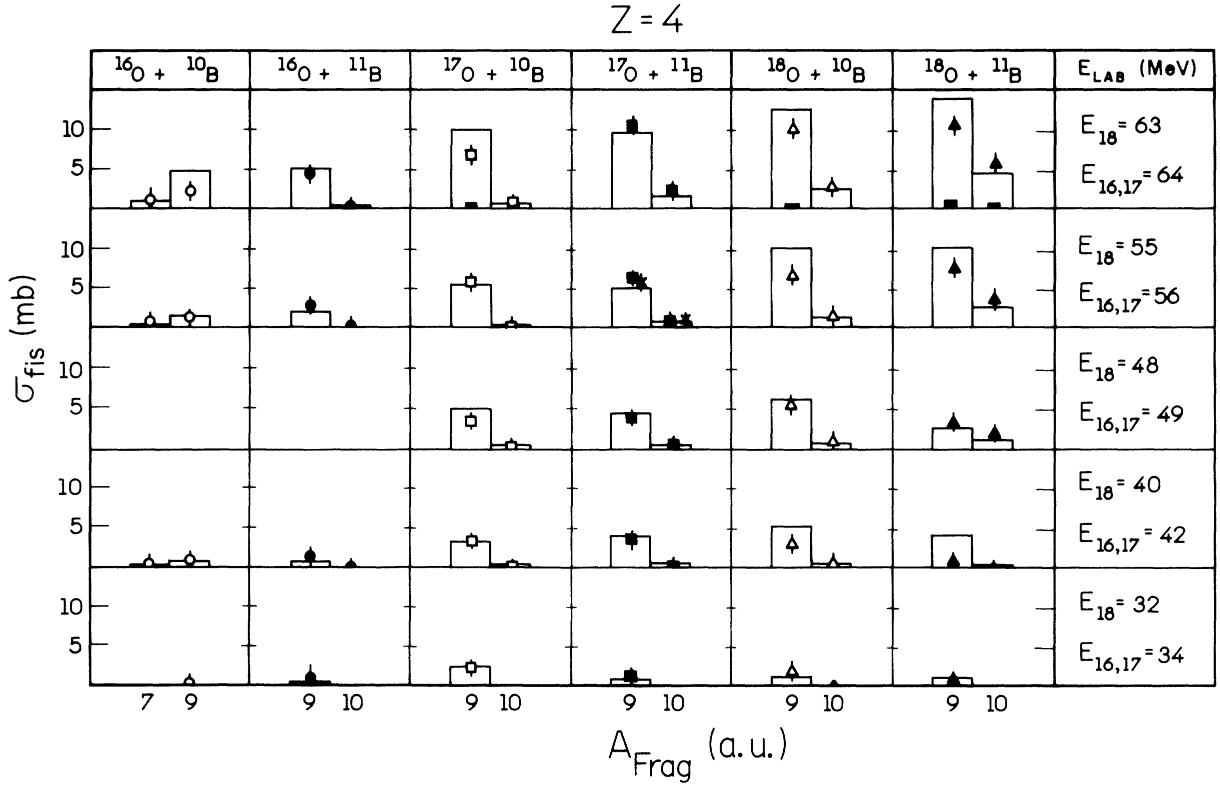

FIG. 21. Same as Fig. 19 for beryllium.

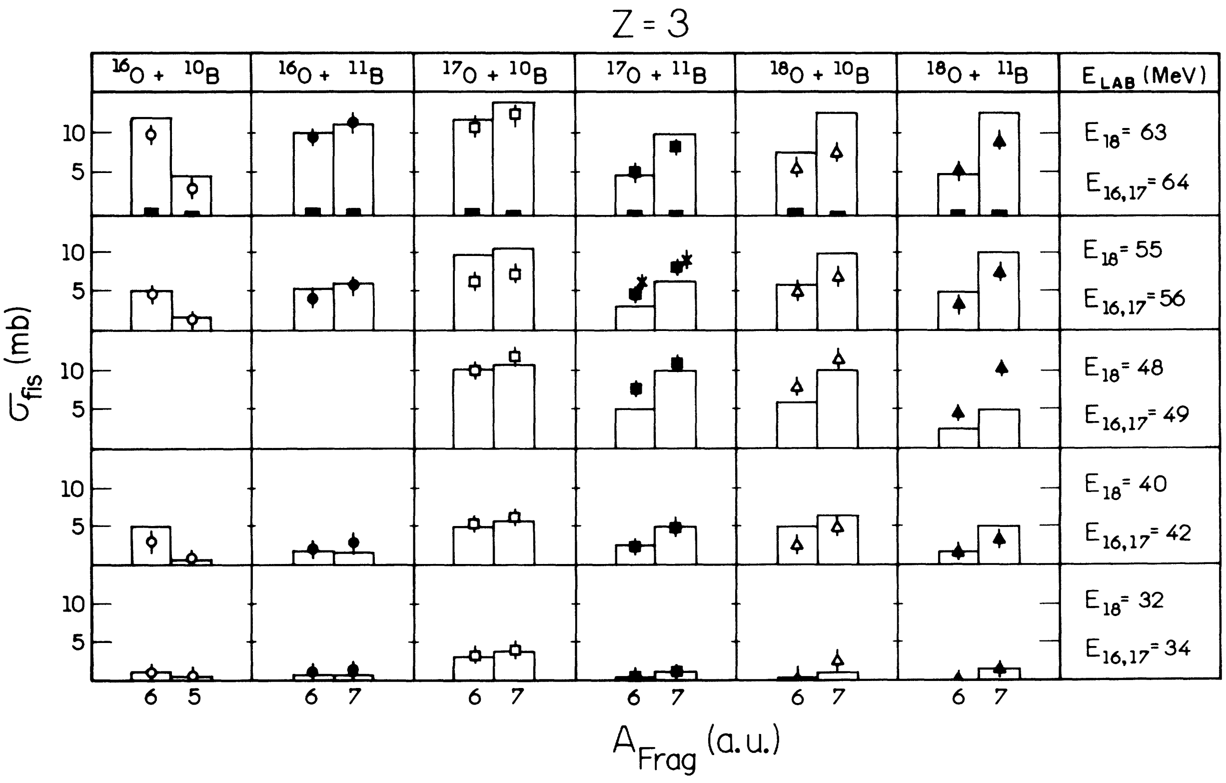

FIG. 22. Same as Fig. 19 for lithium.

Bass description of this function [35,36]. This is shown by the shaded area in Fig. 23.

We adjust the parameters in order to reproduce with a reasonable agreement the experimental fusion cross section, and in doing so, we extract the predicted orbiting cross sections (see Figs. 19–22).

C. Number of open channels

Either the fusion-fission reaction or orbiting processes are dominated, in the angular momentum space, by the highest-l partial waves, located around the l grazing. Therefore it is important to calculate the number of open channels (NOC) available to carry away the grazing angular momentum l_g of the composite system. Studies reported in the literature [12,37] have shown for several systems a strong correlation between the existence of very low NOC and the occurrence of resonant behavior and back-angle enhancement in the elastic, inelastic, or α-transfer channels. These systems, basically composed of α nuclei, presented the important deep-inelastic orbiting yields.

The NOC has been calculated for the systems investigated in the present work, as well as for the ^{12}C+^{12}C and ^{12}C+^{16}O systems (see Fig. 24). The NOC is determined by the Hauser-Feshbach denominator for the grazing partial wave. The level density of states available is described by the Fermi-gas expression. Namely, the number of open channels per unit of incident flux is given by

$$(N/F)_{l_g} = \frac{\sum_{b'} \int_0^{E_{\max}} \rho_b(E,I)_l T_l^{\text{out}}(E)_l dE}{\pi \lambda\!\!\!^{-2} \sum_l (2l+1) T_l^{\text{in}}} \, . \quad (8)$$

The ^{12}C+^{12}C and ^{12}C+^{16}O systems show very low minimum values ($\approx 10^{-1}$). This is consistent with the prominent resonant behavior clearly described for these systems [12,38] and for which important orbiting yields may be expected. On the other hand, the B+O systems show much higher values for the NOC. In the case of heavier systems, strongly energy-damped yields produced by reaction with large NOC have been associated with the occurrence of fusion-fission processes [37]. The large phase space available for the decay of the O+B system (e.g., $\approx 10^4$ times larger than in the C+C case) further supports the fusion-fission picture for the origin of the binary energy-damped yields.

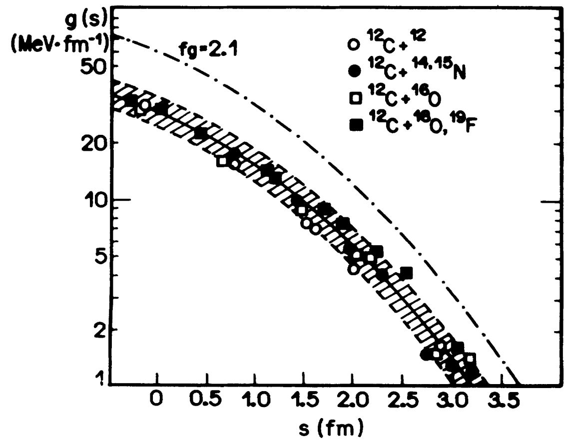

FIG. 23. Bass potential parameter $g(s)$ used in the calculations of the "orbiting yields."

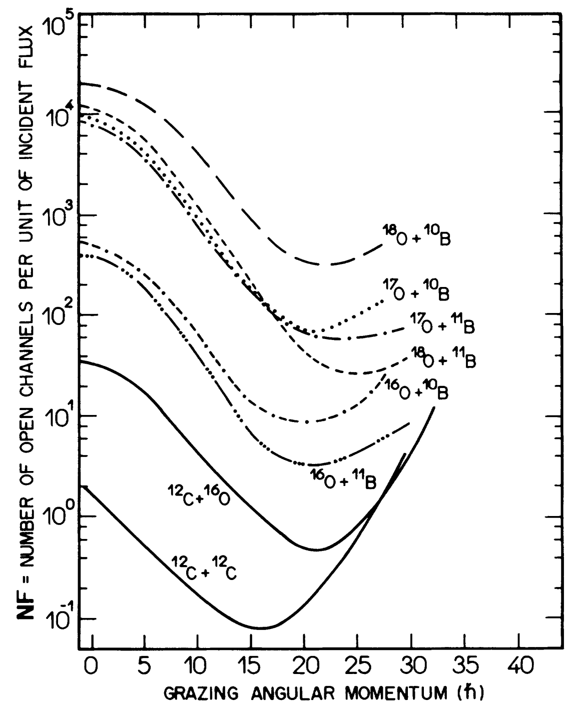

FIG. 24. Number of open channels for the decay of the compound nucleus normalized to the incident flux, as a function of the entrance-channel grazing angular momentum.

VI. CONCLUSIONS

The ^{16,17,18}O+^{10,11}B and ^{19}F+^{9}Be reactions have been investigated over a wide energy regime. Elastic, strongly energy-damped, and evaporation yields were determined using both singles and coincidence measurements. The coincidence data were particularly useful in helping to characterize the binary component of the reaction yields.

Results presented in this work indicate that statistically equilibrated compound nuclei formed in these reactions can decay by either light-particle emission or binary fission. The observed yields are shown to be consistent with statistical-model predictions. No evidence is found for an incomplete-fusion process at the energies measured. The analysis of the elastic-scattering back-angle cross section based on Hauser-Feshbach calculations suggests an important contribution of the compound-elastic yields. This is consistent with the evidence for significant binary-fission yield.

The excitation functions of fusion-fission cross sections in the (B+O)* channel as well as compound-elastic cross sections allow one to determine, as shown in Fig. 25, the "inelastic fission" barriers ($V_{F'}$) as well as compound-

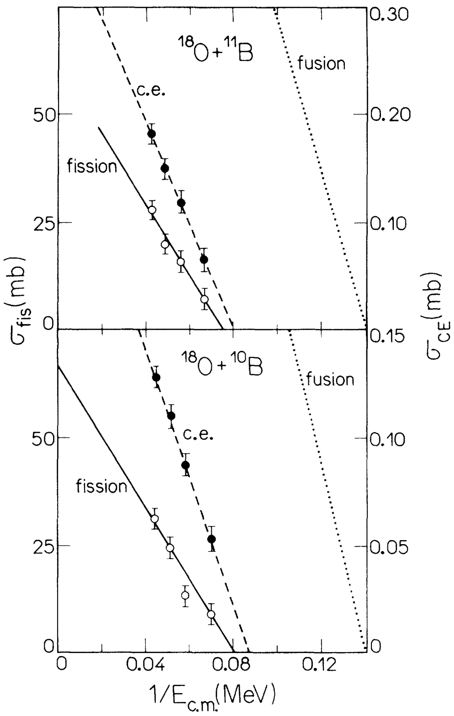

FIG. 25. Total compound elastic and fission cross section for the (B+O)* channel as a function of $1/E_{\mathrm{c.m.}}$.

elastic or an "elastic fission" barrier V_F associated with the threshold for production of inelastic binary products and compound-elastic yields, respectively (see Table IV). The consistency of those values further supports the picture proposed for the reaction mechanism.

TABLE IV. Experimental values for "elastic fission barriers" (V_B) and "inelastic" fission barriers ($V_{F'}$).

System	V_F (MeV)	$V_{F'}$ (MeV)
^{16}O+^{10}B	12.5±1.0	13.9±0.9
^{16}O+^{11}B	13.7±1.0	14.8±1.0
^{17}O+^{10}B	13.0±1.2	13.5±0.9
^{17}O+^{11}B	13.4±1.0	14.5±0.7
^{18}O+^{11}B	11.7±0.9	12.7±0.6
^{18}O+^{11}B	12.5±0.8	13.3±0.6

Satisfactory fits were obtained for our data, both for evaporation residues and mainly for fusion-fission products, expanding the validity of statistical and liquid drop models for such light systems [39]. The success of the transition-state model in describing such processes, as shown in Figs. 17 and 19–22, supports the applicability of statistical models in very light nuclear configurations. These results suggest the possibility of investigation of highly deformed configurations in very light nuclear systems.

ACKNOWLEDGMENTS

This work has been partially supported by Conselho Nacional de Desenvolvimento Científico e Tecnológico (CNPq) and Fundação de Amparo à Pesquisa do Estado de São Paulo (FAPESP). One of us (S.J.S.) would like to acknowledge the support of the U.S. Department of Energy, Nuclear Science Division, under Contract No. DE-FG02-89ER40506.

---

[1] A. Szanto de Toledo, M. M. Coimbra, N. Added, R. M. Anjos, N. Carlin Filho, L. Fante, Jr., M. C. S. Figueira, V. Guimarães, and E. M. Szanto, Phys. Rev. Lett. **62**, 1255 (1989).
[2] A. Szanto de Toledo, L. Fante, Jr., R. M. Anjos, N. Added, M. M. Coimbra, M. C. S. Figueira, N. Carlin Filho, E. M. Szanto, M. S. Hussein, and B. V. Carlson, Phys. Rev. C **42**, R815 (1990).
[3] S. J. Sanders, R. R. Betts, I. Ahmad, K. T. Lesko, S. Saini, B. D. Wilkins, F. Videbaek, and B. K. Dichter, Phys. Rec. C **34**, 1746 (1986).
[4] S. J. Sanders, D. G. Kovar, B. B. Back, C. Beck, B. K. Dichter, D. Henderson, R. V. F. Janssens, J. G. Keller, S. Kaufman, T. F. Wang, B. Wilkins, and F. Videback, Phys. Rev. Lett. **59**, 2856 (1987).
[5] S. J. Sanders, D. G. Kovar, B. B. Back, C. Beck, D. J. Henderson, R. V. F. Janssens, T. F. Wang, and B. D. Wilkins, Phys. Rev. C **40**, 2091 (1989).
[6] S. J. Sanders, B. B. Back, R. V. F. Janssens, D. G. Kovar, D. Habs, D. Henderson, T. L. Khoo, H. Korner, G. E. Rathke, T. F. Wang, F. L. H. Wolfs, and K. B. Bear, Phys. Rev. C **41**, R1901 (1990).
[7] C. Beck, B. Djerroud, B. Heusch, R. Dayras, R. M. Freeman, F. Haas, A. Hachem, J. P. Wieleczko, and M. Youlal, Z. Phys. A **334**, 521 (1989).
[8] C. Beck, B. Djerroud, F. Haas, R. M. Freeman, A. Hachem, B. Heusch, A. Morsad, M. Youlal, Y. Abe, R. Dayras, J. P. Wieleczko, T. Matsuse, and S. M. Lee, Z. Phys. A **334**, 521 (1989).
[9] D. Shapira, R. Novotny, Y. D. Chan, K. A. Erb, J. J. L. C. Ford, J. C. Peng, and J. D. Moses, Phys. Lett. **114B**, 111 (1982).
[10] D. Shapira, Phys. Rev. Lett. **61**, 2153 (1988).
[11] A. Ray, D. Shapira, J. Gomez del Campo, H. J. Kim, C. Beck, B. Djerroud, D. Blumenthal, and B. Shivakumar, Phys. Rev. C **44**, 514 (1991).
[12] A. Ray, D. Shapira, Y. Abe, S. M. Lee, and F. Sakata, in *Towards a Unified Picture of Nuclear Dynamics*, Nikko, Japan, AIP Conf. Proc. No. 250, edited by Y. Abe, S. M. Lee, and S. Sakata (AIP, New York, 1991), p. 55.
[13] A. Ray, S. Gil, M. Khandaker, D. D. Leach, D. K. Lock, and R. Vandenbosch, Phys. Rev. C **31**, 1573 (1985).
[14] A. Ray, D. D. Leach, R. Vandenbosch, K. T. Lesko, and D. Shapira, Phys. Rev. Lett. **57**, 815 (1986).
[15] R. M. Anjos, N. Added, N. Carlin, L. Fante, Jr., M. C. S. Figueira, R. Matheus, E. M. Szanto, C. Tenreiro, A. Szanto de Toledo, H. R. Schelin, and S. J. Sanders, Phys. Rev. C **48**, R2154 (1993).
[16] L. Fante, Jr., N. Added, R. M. Anjos, N. Carlin, M. M. Coimbra, M. C. S. Figueira, R. Matheus, E. M. Szanto,

and A. Szanto de Toledo, Nucl. Phys. **A552**, 82 (1993).

[17] M. M. Coimbra, R. M. Anjos, N. Added, N. Carlin, L. Fante, Jr., M. C. S. Figueira, G. Ramirez, E. M. Szanto, and A. Szanto de Toledo, Nucl. Phys. **A535**, 161 (1991).

[18] M. S. Hussein, A. N. Aleixo, L. F. Canto, P. Carrilho, R. Donangelo, and L. S. de Paula, J. Phys. **13**, 967 (1987).

[19] A. Lépine-Szily, J. M. Oliveira, Jr., P. Fachini, R. Lichtenthäler Filho, M. M. Obuti, W. Sciani, M. K. Steinmayer, and A. C. C. Villari, Nucl. Phys. **A539**, 487 (1992).

[20] R. G. Stokstad, computer code STATIS, Yale University, Report No. 52, 1972.

[21] N. Carlin, M. M. Coimbra, J. C. Acquadro, R. Liguori Neto, E. M. Szanto, E. Farrelly-Pessoa, and A. Szanto de Toledo, Phys. Rev. C **31**, 152 (1985).

[22] M. M. Macfarlane and S. C. Pieper, computer code PTOLEMY, Argonne National Laboratory, 1978.

[23] H. Morgenstern, W. Bohne, K. Grabish, H. Lehr, and W. Stöffer, Z. Phys. A **313**, 39 (1983).

[24] J. Gomez del Campo, J. A. Biggerstaff, R. A. Dayras, D. Shapira, A. H. Shell, P. H. Stelson, and R. G. Stokstad, Phys. Rev. C **29**, 1722 (1984).

[25] Y. D. Chan, D. E. di Gregorio, J. L. C. Ford, Jr., J. Gomez del Campo, M. E. Ortiz, and D. Shapira, Phys. Rev. C **25**, 1410 (1982).

[26] D. Glas and U. Mosel, Phys. Lett. **49B**, 301 (1974).

[27] C. K. Gelbke *et al.*, Phys. Rep. **42**, 311 (1978), and references therein.

[28] C. Beck, D. Djerroud, F. Haas, R. M. Freeman, A. Hachem, B. Heusch, A. Morsad, and M. Vuillet-A-Cilles (private communication).

[29] S. J. Sanders, D. G. Kovar, B. B. Back, C. Beck, B. K. Dichter, D. Henderson, R. V. F. Janssens, J. G. Keller, S. Kaufman, T. F. Wang, B. Wilkins, and F. Videbaeck, Phys. Rev. Lett. **61**, 2154 (1988).

[30] S. J. Sanders, Phys. Rev. C **44**, 2676 (1991).

[31] B. Shivakumar, S. Ayik, B. A. Harmons, and D. Shapira, Phys. Rev. C **35**, 1730 (1987).

[32] D. Shapira, J. J. L. C. Ford, J. del Campo, R. G. Stokstad, and R. M. de Vries, Phys. Rev. Lett. **43**, 1781 (1979).

[33] F. Puhlöffer, Nucl. Phys. **A280**, 267 (1977).

[34] P. Möller and J. R. Nix, At. Data Nucl. Data Tables A **26**, 165 (1981).

[35] R. Bass, Nucl. Phys. **A231**, 45 (1974).

[36] R. Bass, Phys. Rev. Lett. **39A**, 265 (1977).

[37] F. Haas and Y. Abe, Phys. Rev. Lett. **46**, 1667 (1981).

[38] T. M. Cormier, Annu. Rev. Nucl. Sci. **32**, 271 (1982).

[39] A. Szanto de Toledo, E. M. Szanto, M. Wotfe, B. V. Carlson, R. Donangelo, W. Bohne, K. Grabish, H. Morgenstern, and S. Proshitzki, Phys. Rev. Lett. **70**, 2070 (1993).